



Research article

A computational study on the influence of aortic valve disease on hemodynamics in dilated aorta

Lijian Xu^{1,2}, Lekang Yin³, Youjun Liu⁴ and Fuyou Liang^{1,2,*}

¹ School of Naval Architecture, Ocean and Civil Engineering, Shanghai Jiao Tong University, 800 Dongchuan Road, Shanghai 200240, China

² Collaborative Innovation Center for Advanced Ship and Deep-Sea Exploration (CISSE), Shanghai Jiao Tong University, 800 Dongchuan Road, Shanghai 200240, China

³ Department of Radiology, Shanghai Chest Hospital, Shanghai 200030, China

⁴ College of Life Science and Bioengineering, Beijing University of Technology, Beijing, 100124, China

* **Correspondence:** Email: fuyouliang@sjtu.edu.cn; Tel: +862134205120; Fax: +862134207804.

Abstract: A computational hemodynamics method was employed to investigate how the morphotype and functional state of aortic valve would affect the characteristics of blood flow in aortas with pathological dilation, especially the intensity and distribution of flow turbulence. Two patient-specific aortas diagnosed to have pathological dilation of the ascending segment while differential aortic valve conditions (i.e., one with a stenotic and regurgitant RL bicuspid aortic valve (RL-BAV), whereas the other with a quasi-normal tricuspid aortic valve (TAV)) were studied. When building the computational models, in addition to in vivo data-based reconstruction of geometrical model and boundary condition setting, the large eddy simulation method was adopted to quantify potential flow turbulence in the aortas. Obtained results revealed the presence of complex flow patterns (denoted by time-varying changes in vortex structure), flow turbulence (indicated by high turbulent eddy viscosity (TEV)), and regional high wall shear stress (WSS) in the ascending segment of both aortas. Such hemodynamic characteristics were significantly augmented in the aorta with RL-BAV. For instance, the space-averaged TEV in late systole and the wall area exposed to high time-averaged WSS (judged by $WSS > \text{two times of the mean WSS in the entire aorta}$) in the ascending aortic segment were increased by 176% and 465%, respectively. Relatively, flow patterns in the descending aortic segment were less influenced by the aortic valve disease. These results indicate that aortic valve disease has profound impacts on flow characteristics in the ascending aorta, especially the distribution and degree of high WSS and flow turbulence.

Keywords: aortic dilation; aortic valve disease; flow turbulence; computational model; large eddy simulation

1. Introduction

Pathological dilation of the ascending aorta is a common aortic disease, which, if untreated, may progressively weaken aortic wall and lead to the formation of aortic dissection/aneurysm or even sudden rupture [1,2]. In clinical practice, the maximum diameter of aorta is usually taken as the main indicator for decision-making [3], although there is increasing evidence that the morphotype of aortic valve is an important factor associated with the risk and progression of aortic dilation [4–10]. It has been found that the incidence of aortic dilation or aneurysm formation in patients with bicuspid aortic valve (BAV) is 50% to 70% [4], and that patients with BAV often have larger aortic root dimensions and a higher progression rate of dilation in comparison with patients with a normal tricuspid aortic valve (TAV) [5,6]. Numerous *in vivo* or *in vitro* studies have demonstrated that hemodynamic characteristics in aortas with BAV not only differ remarkably from those in aortas with TAV, but also depend strongly on the morphotype of BAV [7–12]. The fusion configuration of valve cusps provides an anatomical basis for the categorization of BAV and explaining the associated characteristics of aortic hemodynamics. For instance, in cases of RL-BAV with fusion of the right and left coronary cusps, the flow jet through the aortic valve is directed toward the right anterior wall of the ascending aorta, leading to elevated wall shear stress (WSS) in this region; whereas in cases of RN-BAV with fusion of the right and noncoronary cusps, the flow jet is directed toward the posterior wall of the ascending aorta, making the distribution of high WSS differ significantly from those observed in aortas with RL-BAV [9–12]. Despite the useful insights from these studies, detailed quantification of hemodynamic parameters using *in vivo* measurement or *in vitro* experimental methods remains challenging due to issues related to the limited spatio-temporal resolutions of available measurement techniques.

In this context, computational fluid dynamics (CFD) methods have been widely employed to quantitatively study the characteristics of aortic hemodynamics in the context of various aortic valve abnormalities (e.g., anomaly, stenosis, and regurgitation) [13–16]. A major advantage of CFD methods is their high precision in computing near-wall hemodynamic parameters that are considered to be associated closely with the pathophysiology of vascular wall while challenging for *in vivo* measurement. On the other hand, the fidelity of a CFD model in reproducing *in vivo* hemodynamics is affected by a variety of factors involved in model setup. For instance, it has been found that imposing idealized flow velocity profiles at the inlets of patient-specific aortic models causes significant deviations of model outputs from real *in vivo* hemodynamic conditions [17–19], which highlights the importance of patient-specifically prescribing model boundary conditions. Another important issue is relevant to the assumption on the physical properties of blood flow and the corresponding choice of fluid dynamics modeling method. While laminar flow assumption is usually considered to be valid for blood flows in human arteries and has been widely adopted in computational model-based studies on aortic blood flow [18–21], *in vivo* measurements have revealed the presence of highly disturbed unstable flows even in the aortas of healthy subjects [22,23] and the occurrence of marked flow turbulence (confirmed through Fourier decomposition of point-wise flow velocity waveform) in the ascending aortas of patients with aortic valve diseases [22]. In

addition, *in vitro* experiments have shown that RL- and NL-BAVs generate high degrees of flow turbulence in the ascending aorta with normal anatomy [12]. Given that lumen enlargement in aortic dilation tends to reduce mean flow velocity [7], one may ask whether flow turbulence would occur in dilated aortas as well and how the morphotype and functional state of aortic valve would affect the intensity and spatial distribution of flow disturbance. To quantify flow turbulence with CFD methods, direct numerical simulation (DNS) could be the most reliable approach since it can theoretically resolve all spatial and temporal scales of both laminar and turbulent flows, however, DNS is extremely draconian in terms of the requirements for mesh quality, hardware resource and computation time [24,25], and hence is generally impractical to study blood flows in anatomically realistic arteries. Relatively, computational methods based on Reynolds-averaged Navier–Stokes (RANS) models are computationally much cheaper, but are limited by their relatively poor performance in predicting laminar-turbulent transition [26,27]. Lying between DNS and RANS methods is the LES method, which has been demonstrated to provide predictions agreeing well with experimental data for flows with Reynolds numbers in the range of arterial blood flow [28–30], and has been employed to simulate flow turbulence in various pathophysiological scenarios of aortic hemodynamics [29,30].

In the present study, a LES-based computational method was employed to simulate blood flow patterns and flow turbulence in two aortas with pathological dilation of the middle ascending aortic segment while differential aortic valve conditions. Computed results for the two aortas were compared to assess the influence of aortic valve disease on aortic hemodynamics, especially the intensity and spatial distribution of flow turbulence. When building the computational models, *in vivo* flow information derived from phase contrast magnetic resonance imaging (PC-MRI) data was used to prescribe model boundary conditions so as to improve the fidelity of computer models in reproducing patient-specific hemodynamics. In the meantime, four-dimensional magnetic resonance imaging (4D-MRI) data of *in vivo* aortic blood flow were acquired and used as a reference for validating the results of hemodynamic simulations.

2. Materials and method

2.1. Acquisition of clinical data

Two patients diagnosed to have aortic dilation at the middle ascending segment were enrolled in the study upon ethical approval and the receipt of patient consent. Besides aortic dilation, the patients were found to suffer from various types and severities of aortic valve abnormality. One patient (patient #1) had a RL-BAV with severe stenosis (mean pressure gradient: 43 mm Hg) and moderate regurgitation (regurgitant fraction: 42.86%), while the other patient (patient #2) had a quasi-normal TAV with mild regurgitation (regurgitant fraction: 8.24%). Diagnosis of aortic valve stenosis or regurgitation was based on transthoracic echocardiographic and PC-MRI data. Detailed demographic information of the patients and the basic geometrical and hemodynamic parameters of the aortas and aortic valves are summarized in Table 1. Chest CTA (computed tomography angiography) and ECG-gated PC-MRI examinations were performed in sequence on each patient with a 64-channel multi-detector CT scanner (Philips Healthcare, The Netherlands) and a 3T MR scanner (Philips Healthcare, The Netherlands), respectively. During PC-MRI scanning, oblique sagittal MR slices were aligned with the aortic inlet and selected cross-sections of aortic branch arteries so that the

measured flow velocity information can be used to prescribe the boundary conditions of CFD model. In addition, flow velocity information in the entire aorta was also acquired through isotropic spatial sampling of flow field (field of view = $300 \times 350 \text{ mm}^2$, voxel size = $2.5 \times 2.5 \text{ mm}^2$, slice thickness = 2.5 mm) using flow-sensitive 4D-MRI and visualized with the Circle Cardiovascular Imaging software (CVI, Calgary, Alberta, Canada).

Table 1. Baseline information of patients and main geometrical and hemodynamic parameters of the aortas and aortic valves.

	Patient #1	Patient #2
Age	77	61
Sex	Male	Female
Heart rate (bpm)	70	56
Aortic disease	Mid-ascending aortic dilation	Mid-ascending aortic dilation
Morphology of aortic valve	RL-BAV	TAV
Aortic valve stenosis	Severe	None
Aortic valve regurgitation	Moderate	Mild
Mean pressure gradient (mmHg)	43.0	7.0
Regurgitant fraction (%)	42.86	8.24
Maximum diameter of aorta (mm)	45	52
Diameter of aortic inlet (mm)	38	38
Severity of aortic dilation [#]	1.18	1.37
Mean Re at aortic inlet	521	922
Peak Re at aortic inlet	3257	4342
Wo at aortic inlet	27.86	24.96

Abbreviations: BAV, bicuspid aortic valve; RL, right-left fusion; TAV, tricuspid aortic valve; Re, Reynolds number; Wo, Womersley number. [#]assessed by maximum-to-aortic-inlet diameter ratio

2.2. Image-based geometrical model reconstruction and mesh generation

The CTA images (which have a slice spacing of 0.4 mm and a spatial resolution of 512×512 pixels) of each patient were segmented in Mimics 15.0 (Materialise, Belgium) to reconstruct a geometrical model of the aorta and its main branch arteries (see Figure 1(a)). The reconstructed geometrical model was subsequently imported into ICEM CFD 16.0 to generate a high-resolution mesh model. Herein, the fluid domain was firstly divided by tetrahedral elements with a minimum size of 0.4 mm, followed by a mesh refinement treatment in which multiple layers of prism elements were mapped along the vascular wall to improve the precision of flow computation in the near-wall regions (Figure 1(b)). The thickness of the initial prism layer was set to 30 μm (which allows the

dimensionless wall distance y^+ to be always below 1.0 under the simulated flow conditions, fulfilling the requirement of mesh size nearest to the wall in LES), and was increased exponentially toward the interior until the thickness of the last layer approached the size of tetrahedral elements in the interior domain. Mesh sensitivity analyses were conducted on the two aortic models by varying the minimum size of tetrahedral elements from 0.5 mm to 0.4 mm and 0.2 mm. The results showed that the differences in computed space-mean wall shear stress and oscillatory shear index in the ascending aortic segment between the median and finest mesh models were less than 1%. Therefore, adopting a minimum tetrahedral element size of 0.4 mm was considered sufficient to yield numerically acceptable results. The mesh models of the two aortas contained 5592372 and 7061034 elements, respectively.

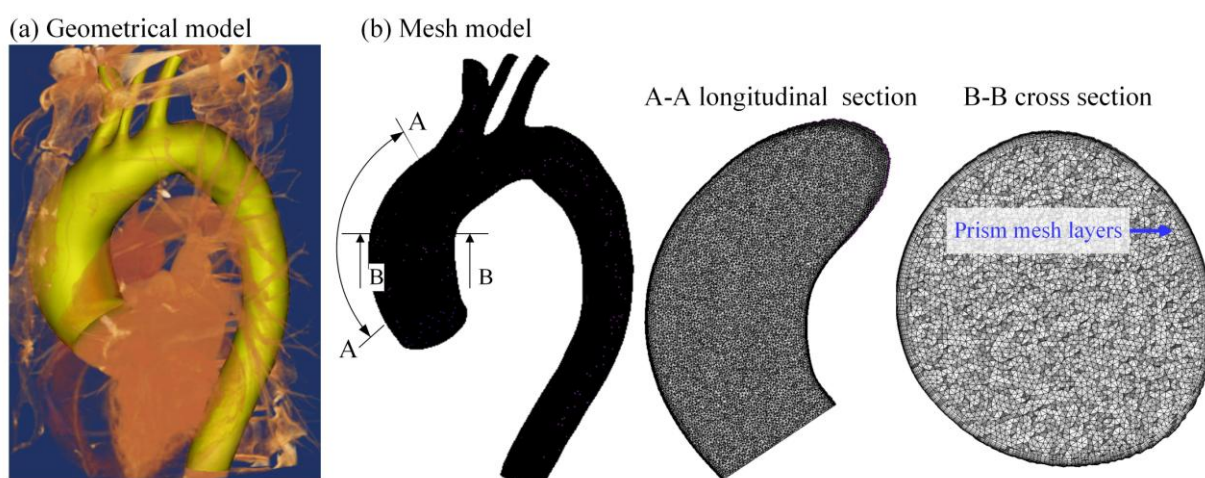


Figure 1. CTA image-based model reconstruction: (a) reconstructed geometrical model for the aorta of patient #1; (b) outside view of the mesh model and longitudinal/cross-sectional views of internal tetrahedral elements and prism layers mapped along the wall.

2.3. Modeling methods for blood flow

Aortic blood flow was assumed to be an incompressible fluid with a constant density of 1055 kg/m^3 governed by the unsteady mass conservation and Navier-Stokes (N-S) equations. The classical Carreau model was employed to dynamically relate blood viscosity to shear rate so as to account for the non-Newtonian rheology of blood [31]. In addition, vascular walls were assumed to be rigid to which the non-slip boundary conditions were imposed.

While the mass conservation and N-S equations can theoretically describe both laminar flow and turbulent flow at an arbitrary point in the flow field, when they are discretized and numerically solved on a mesh model with finite element size, a problem arises as to how sub-grid flow should be represented. In the case of strictly laminar flow, flow variables can generally be assumed to be homogeneous within each individual element [32], the assumption may however lead to considerable numerical errors when applied to turbulent flow due to the presence of sub-grid turbulent eddies smaller in size than the element that will induce non-negligible intra-element viscous energy loss. Therefore, we employed the LES method to account for intra-element viscous energy loss associated

with potential flow turbulence. In the LES method, flow velocity (u_i) in an arbitrary element is separated into a grid-resolved component (\bar{u}_i) and a sub-grid component (u'_i) [33]. In the fluid domain of a mesh model, the grid-resolved velocity components depict the large-scale flow patterns, while the sub-grid velocity components account for the effects of turbulent eddies whose scales are smaller than the grid size.

$$u_i = \bar{u}_i + u'_i. \quad (1)$$

With the above flow velocity separation, the mass conservation and N-S equations can be rewritten as

$$\frac{\partial \bar{u}_i}{\partial x_i} = 0, \quad (2)$$

$$\frac{\partial \bar{u}_i}{\partial t} + \bar{u}_j \frac{\partial \bar{u}_i}{\partial x_j} = -\frac{1}{\rho} \frac{\partial \bar{p}}{\partial x_i} + \frac{\partial}{\partial x_j} \left(\nu \frac{\partial \bar{u}_i}{\partial x_j} \right) + \frac{1}{\rho} \frac{\partial \tau_{ij}}{\partial x_j}, \quad (3)$$

where τ_{ij} is the sub-grid stress tensor that accounts for the dissipative effect of small scale eddies, and is by definition expressed as

$$\tau_{ij} = \overline{u_i u_j} - \bar{u}_i \bar{u}_j. \quad (4)$$

To facilitate numerical solution, τ_{ij} is often related to the large-scale strain rate via an assumed turbulent eddy viscosity (TEV) [33]

$$\tau_{ij} - \frac{\delta_{ij}}{3} \tau_{kk} = -2\nu_t \bar{S}_{ij}, \quad (5)$$

where δ_{ij} is the Kronecker symbol, ν_t is the turbulent eddy viscosity, and \bar{S}_{ij} is the strain rate tensor of the grid-resolved velocity field defined as

$$\bar{S}_{ij} = \frac{1}{2} \left(\frac{\partial \bar{u}_i}{\partial x_j} + \frac{\partial \bar{u}_j}{\partial x_i} \right). \quad (6)$$

ν_t was estimated with the wall-adapted local eddy-viscosity (WALE) LES model [34]

$$\nu_t = (C_\omega \Delta)^2 \frac{(S_{ij}^d S_{ij}^d)^{3/2}}{(\bar{S}_{ij} \bar{S}_{ij})^{5/2} + (S_{ij}^d S_{ij}^d)^{5/4}}. \quad (7)$$

Herein, C_ω is a coefficient fixed at 0.5 for homogeneous isotropic turbulence, Δ is the cube root of the element volume, and S_{ij}^d is the traceless symmetric part of the square of the velocity gradient tensor

$$S_{ij}^d = \frac{1}{2} (\bar{g}_{ij}^2 + \bar{g}_{ji}^2) - \frac{1}{3} \delta_{ij} \bar{g}_{kk}^2, \text{ with } \bar{g}_{ij}^2 = \bar{g}_{ik} \bar{g}_{kj}, \bar{g}_{ik} = \frac{\partial \bar{u}_i}{\partial x_j}. \quad (8)$$

2.4. Patient-specific prescription of model boundary conditions based on PC-MRI data

Physiologically, the spatial distribution of flow velocity at the aortic inlet is highly complex and prone to change with time due to the dynamic hemodynamic interactions among the left ventricle, aortic valve and aorta. It has been extensively demonstrated that imposing an idealized (e.g., plug, parabolic, or Womersley) flow velocity profile at the aortic inlet may cause the model predictions to deviate significantly from in vivo hemodynamics, especially in the ascending aortic region [19,20]. In this study, we extracted the time-varying velocity vector information (including the trans-plane normal velocity component and in-plane tangential velocity component) at the aortic inlet based on the PC-MRI data acquired from each patient and projected the extracted velocity data to the mesh model using an in-house code written in MATLAB according to the methodology proposed in a previous study [35] (see Figure 2(b) for the volumetric flow rate waveform and flow velocity distributions at the aortic inlet of patient #1). In this way, the inflow conditions of each aorta were fully patient-specifically prescribed. The inlet boundary conditions prescribed for the aortas of the two patients are compared in Figure 3 with respect to volumetric flow rate waveform, trans-plane mean flow velocity waveform, trans-plane maximum flow velocity waveform, and spatial distribution of flow velocity at peak systole. It is evident that flow conditions at the aortic inlet differ remarkably between the two patients in terms of both flow waveform and in-plane flow velocity distribution, demonstrating the necessity of patient-specific boundary condition prescription. As for the prescription of outflow boundary conditions, we imposed the volumetric flow rate waveforms derived from the PC-MRI data measured in each patient to the outlets of the aortic branch arteries (i.e., BCA, brachiocephalic artery; LCCA, left common carotid artery; LSA, left subclavian artery) (see Figure 2(a) & (c) for the locations of the outlets and PC-MRI-measured flow waveforms in patient #1, note that the flow waveforms measured in patient #2 were not shown in order to save space). At the outlet of the descending (DAo) aorta of each patient, although patient-specifically measured flow waveform with PC-MRI was available as well, we prescribed the Neumann type free outflow boundary condition instead of imposing the measured flow waveform directly, mainly because: 1) the Neumann type outflow boundary condition can play a role of absorbing potential numerical errors in the fluid domain when Dirichlet boundary conditions are imposed at the inlet and other three outlets, and 2) the rigid wall assumption renders our model unable to tolerate the phase lag between inflow waveform and the sum of outflow waveforms caused by the deformation of aortic wall under in vivo conditions. The latter is evidenced by the considerable differences between the model-predicted and measured flow waveforms at the DAo outlets of patient #1 and patient #2 (see Figure 4).

2.5. Numerical methods

The governing equations of blood flow were solved along with the boundary conditions using a commercial CFD package (ANSYS CFX 16). Second-order schemes were employed for both spatial discretization and time integration. The numerical time step was fixed at 0.1 ms. At each time step, convergence of numerical solution was judged when the root mean-square residuals of the mass and momentum conservation equations all went below 10^{-5} . Moreover, to eliminate uncertain errors introduced by the estimation of initial conditions that were not known in advance, each set of numerical simulation was continuously run for several cardiac cycles. Our numerical tests showed

that the space-mean value of model-simulated time-averaged wall shear stresses in each aorta changed by less than 0.2% from the fourth to the fifth cardiac cycle, indicating that the numerical solution is close to periodic from the fourth cardiac cycle. Accordingly, the numerical results obtained in the fifth cardiac cycle were analyzed and reported. Numerical simulations were run on a Dell workstation equipped with an Intel Xeon (2.9GHz, 32 CPUs). The total computation times for the two aortic models were 58 and 65 hours, respectively.

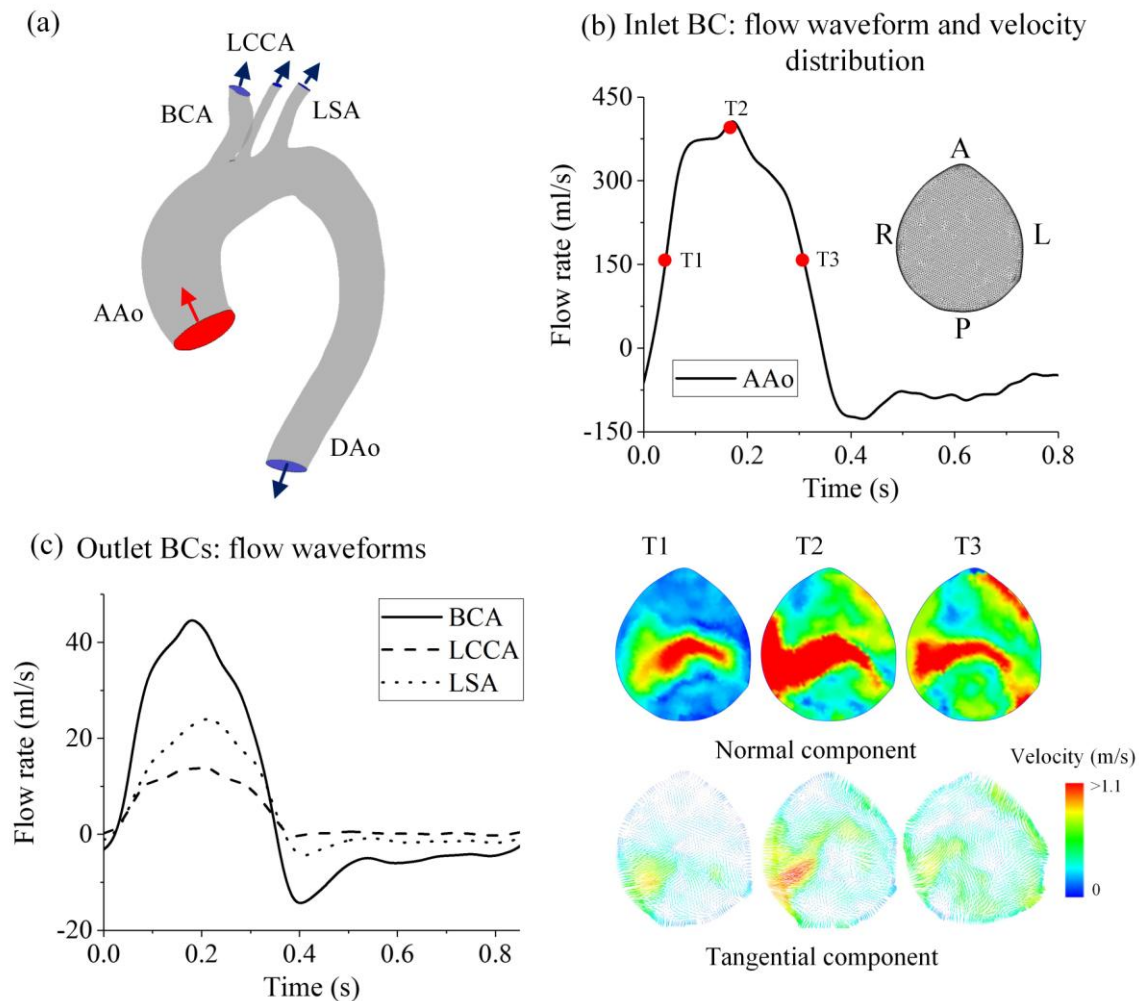


Figure 2. Setup of boundary conditions for the aortic model of patient #1: (a) locations of the inlet (denoted by the red plane) and outlets (denoted by the blue planes) in the model; (b) PC-MRI data-derived volumetric flow waveform (upper panel) and the spatial distributions of the normal and tangential flow velocity components at the model inlet at three time moments in a cardiac cycle (i.e., T1, T2 and T3) (lower panel); (c) PC-MRI data-derived volumetric flow rate waveforms at the outlets of the three branch arteries (i.e., BCA, LCCA, LSA). Abbreviations: AAo, ascending aorta; DAo, descending aorta; BCA, brachiocephalic artery; LCCA, left common carotid artery; LSA, left subclavian artery; BC, boundary condition; A, anterior; P, posterior; R, right; L, left.

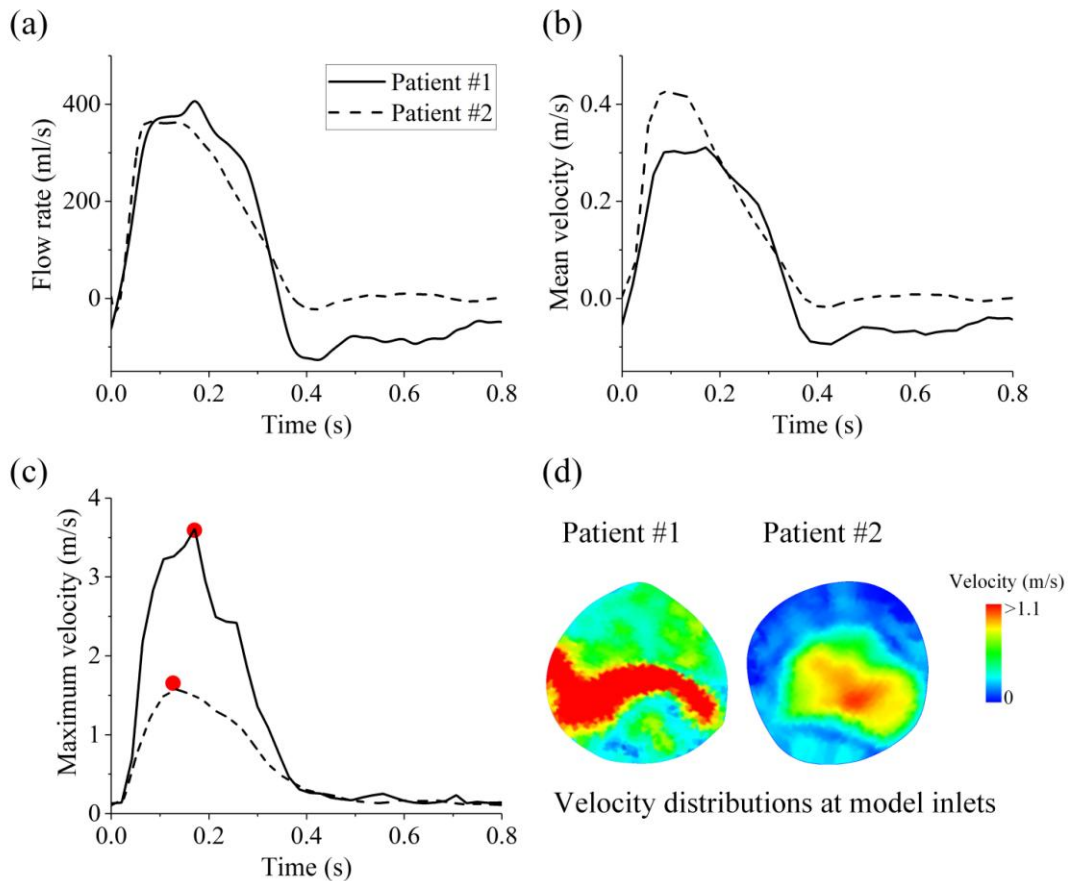


Figure 3. Comparisons of the PC-MRI data-derived inlet boundary conditions between the aortas of the two patients in terms of trans-plane volumetric flow rate waveform (a), mean flow velocity waveform (b), maximum flow velocity waveform (c), and spatial distribution of trans-plane velocity at peak systole (denoted by the filled red circles in panel (c)) (d).

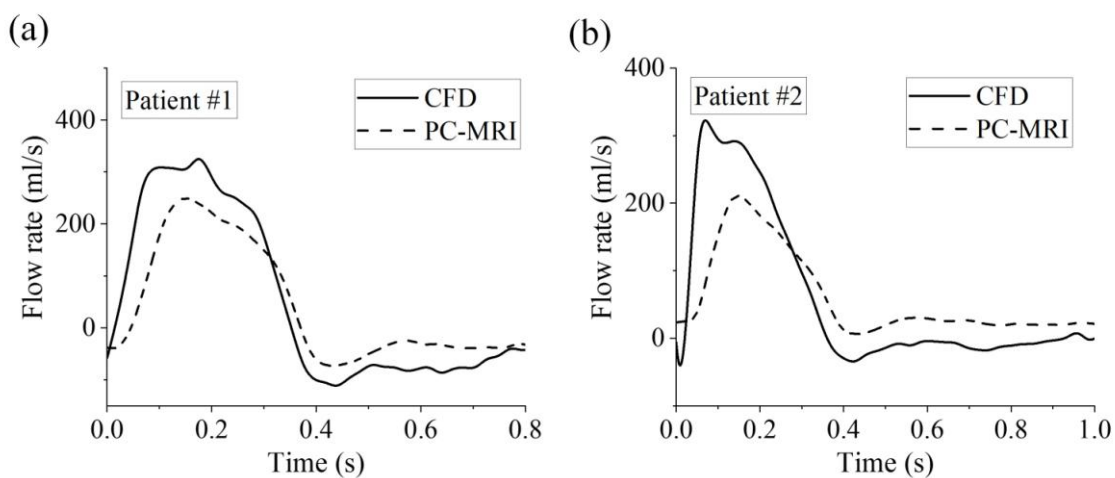


Figure 4. Comparisons between model-predicted and measured (with PC-MRI) flow waveforms at the outlet of descending aorta in patient #1 (a) and patient #2 (b).

2.6. Data analysis

The simulated time-varying WSS vector ($\vec{\tau}_w$) was analyzed over a cardiac cycle (T) to derive the time-averaged wall shear stress (TAWSS) and oscillatory shear index (OSI) that have been extensively proved to be typical hemodynamic parameters associated with arterial disease [19,36,37].

$$\text{TAWSS} = \frac{1}{T} \int_0^T |\vec{\tau}_w| dt, \quad \text{OSI} = \frac{1}{2} \left(1 - \frac{|\int_0^T \vec{\tau}_w dt|}{\int_0^T |\vec{\tau}_w| dt} \right). \quad (9)$$

TAWSS and OSI were further spatially averaged in the ascending or descending aortic segment to facilitate quantitative comparisons of these parameters between the two aortas.

$$\text{SA-TAWSS} = \frac{1}{S_{Ao}} \sum_{i=1}^n \text{TAWSS}_i \cdot \Delta S_i, \quad \text{SA-OSI} = \frac{1}{S_{Ao}} \sum_{i=1}^n \text{OSI}_i \cdot \Delta S_i. \quad (10)$$

Here, S_{Ao} is the total wall area of the aortic segment, i is the index of a mesh surface on the aortic wall that contains a total number of n mesh surfaces, and ΔS_i is the area of the i th mesh surface, with the corresponding TAWSS and OSI being denoted by TAWSS_i and OSI_i , respectively.

Similarly, turbulent eddy viscosity (TEV), which reflects the intensity of flow turbulence in each mesh element, was averaged over the space of ascending or descending aortic segment.

$$\text{SA-TEV} = \frac{1}{V_{Ao}} \sum_{i=1}^n \text{TEV}_i \cdot \Delta V_i, \quad (11)$$

where, V_{Ao} is the total volume of the aortic segment, i is the index of a mesh element with its volume and TEV being denoted by ΔV_i and TEV_i , respectively.

3. Results

Figure 5 shows the model-simulated flow streamlines at three time moments in the aortas of patient # 1 and patient #2 and their comparisons with in vivo 4D-MRI visualizations (videos of the simulated and measured flow streamlines in the aorta of patient #1 are available in the supplementary material). The presence of high-speed jet flows impinging on the anterior wall of the ascending aortic segment was captured by both model prediction and 4D-MRI measurement, which demonstrates the ability of our computational models to reasonably reproduce the main features of in vivo hemodynamics. Nevertheless, when the details of model-simulated and measured flow fields were compared, considerable discrepancies were observed. For instance, the model-predicted flow structures in the ascending aorta were more complex and flow velocities in the descending aorta were higher (especially at T2) in comparison with those presented by the 4D-MRI data. The discrepancies are likely to arise from the inherent limitations of the modeling method and in vivo measurement: 1) the adoption of rigid wall assumption renders our models unable to account for wall deformation and the variations in phase angle and shape of flow waveform along the aorta (see Figure 4) that both considerably affect intra-aortic flow patterns; and 2) the limited spatio-temporal resolutions of 4D-MRI measurement may compromise the visualization of detailed flow patterns, especially in the ascending aortic region where flow field is highly complex and unstable. With regard to the comparison of flow patterns in the two aortas, although high-speed jet flows impinging

on the anterior wall of the ascending aortic segment were detected in both aortas, the area subject to flow impingement was much larger and flow disturbance was stronger in the aorta of patient #1.

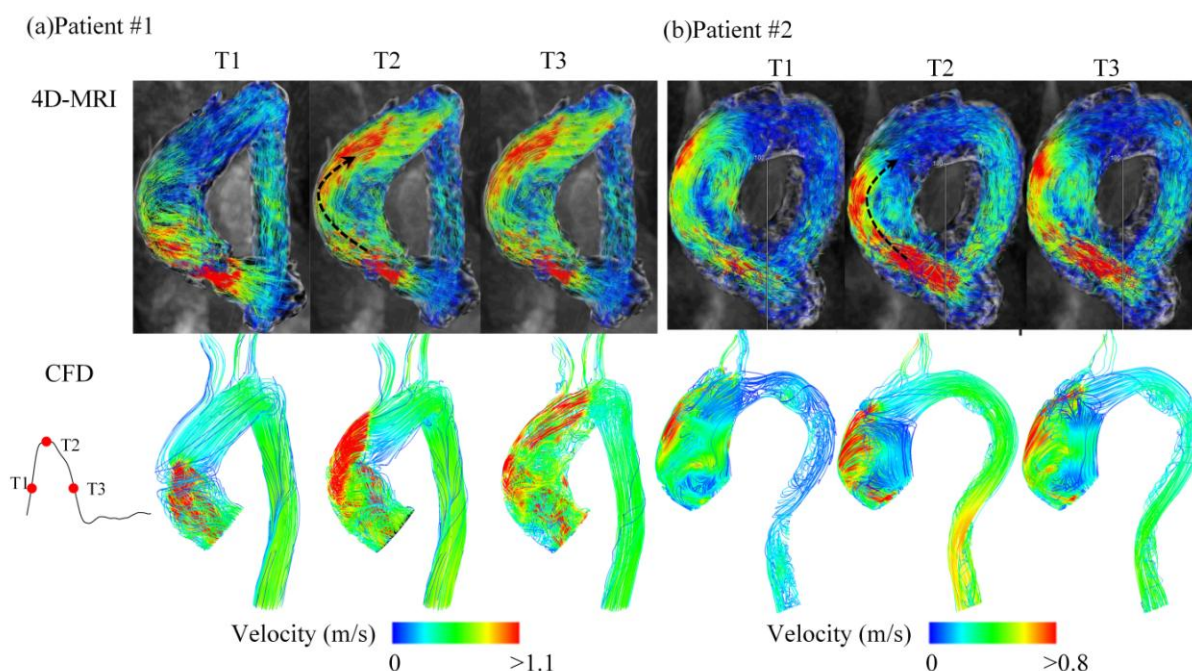


Figure 5. Comparisons of 4D-MRI-visualized aortic flow streamlines at three representative time moments (i.e., T1 (early systole), T2 (peak systole) and T3 (late systole)) with those obtained by numerical simulations for patient #1 (a) and patient #2 (b). The curved arrows indicate the main path of the impingement flows directed from the aortic inlet toward the descending aorta through the anterior region of the ascending aorta.

Figure 6 shows the simulated flow velocity distributions in a transverse plane of the ascending segments of the two aortas at three time moments (i.e., T1 in the acceleration phase, T2 at peak systole, and T3 in the deceleration phase). The corresponding flow velocity distributions in a longitudinal cutting plane are presented in Figure 7. Basically, flows in both aortas were disturbed, asymmetric and time-varying. However, the spatial distribution of velocity and its variation with time differed remarkably between the aortas. For instance, in the ascending aorta of patient #1, high-speed flow jets were observed in the vicinity of both the anterior and right walls, whereas they appeared only in the anterior area of the ascending aorta of patient #2. To further explore the differences in three-dimensional flow patterns and the intensity and distribution of flow turbulence between the two aortas, intra-aortic vortex structures were visualized in form of turbulent eddy viscosity-colored iso-surfaces of Λ_2 (at a level value of 0.05) (see Figure 8). Overall, complex vortex structures and high turbulent eddy viscosity were present mainly in the ascending aortic segment. For both aortas, the complexity of vortex structure and turbulent eddy viscosity changed with time, and were remarkably enhanced in the deceleration phase. When the vortex structure and turbulent eddy viscosity in the deceleration phase (i.e., late systole at T3) were compared between the two aortas, vortex breakdown accompanied by increased turbulent eddy viscosity in the ascending aortic segment was much more pronounced in patient #1 than in patient #2. Accordingly,

the space-averaged turbulence eddy viscosity (SA-TEV) in the ascending aorta of patient #1 was 176% higher than that in patient #2 (see Figure 9). In contrary, the SA-TEV in the descending aortic segment was lower in patient #1 than in patient #2, although the low intensity of flow turbulence (indicated by the small value of TEV) in the descending aortic segment reduces the significance of the comparison.

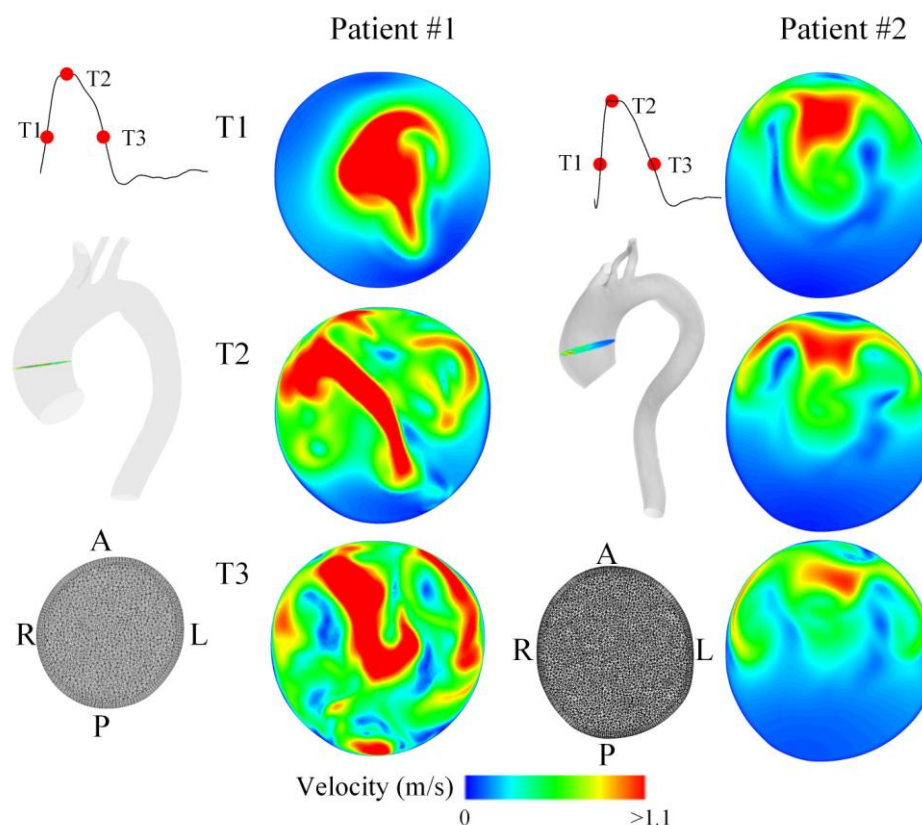


Figure 6. Simulated flow fields (illustrated in form of filled flow velocity contours in a transverse cutting plane at three time moments (i.e., T1, T2 and T3)) in the aortas of patient #1 (left panel) and patient #2 (right panel).

Figure 10 shows the model-predicted distributions of TAWSS and OSI in the two aortas. Regional high TAWSS in the ascending segment was predicted for both aortas, but with its degree and spatial distribution differing considerably between the aortas. Relatively, TAWSS in the descending aortic segment was more evenly distributed. As for the distribution of OSI, considerable difference between the two aortas was observed. For instance, focal high OSI appeared in the entire aorta of patient #1 while only in the ascending segment of the aorta of patient #2. To further quantitatively compare the values of TAWSS and OSI in the two aortas, the space-averaged TAWSS and OSI (i.e., SA-TAWSS, SA-OSI) in the ascending and descending segments of the two aortas are plotted in Figure 11. It is evident that SA-TAWSS in the ascending aortic segment was much larger in patient #1, whereas SA-TAWSS in the descending aortic segment was comparable between the two patients. If a local TAWSS of at least two times of the mean TAWSS over the entire aorta is set as the threshold of high TAWSS, the total area of ascending aortic wall exposed to high TAWSS was 26.1 cm^2 in patient #1, which was much larger than that (4.6 cm^2) in patient #2. The comparison of

SA-OSI between the two aortas however revealed a phenomenon different from that of SA-TAWSS. For instance, ascending aortic SA-OSI was comparable between the two patients, whereas descending aortic SA-OSI was evidently higher in patient #1 than in patient #2.

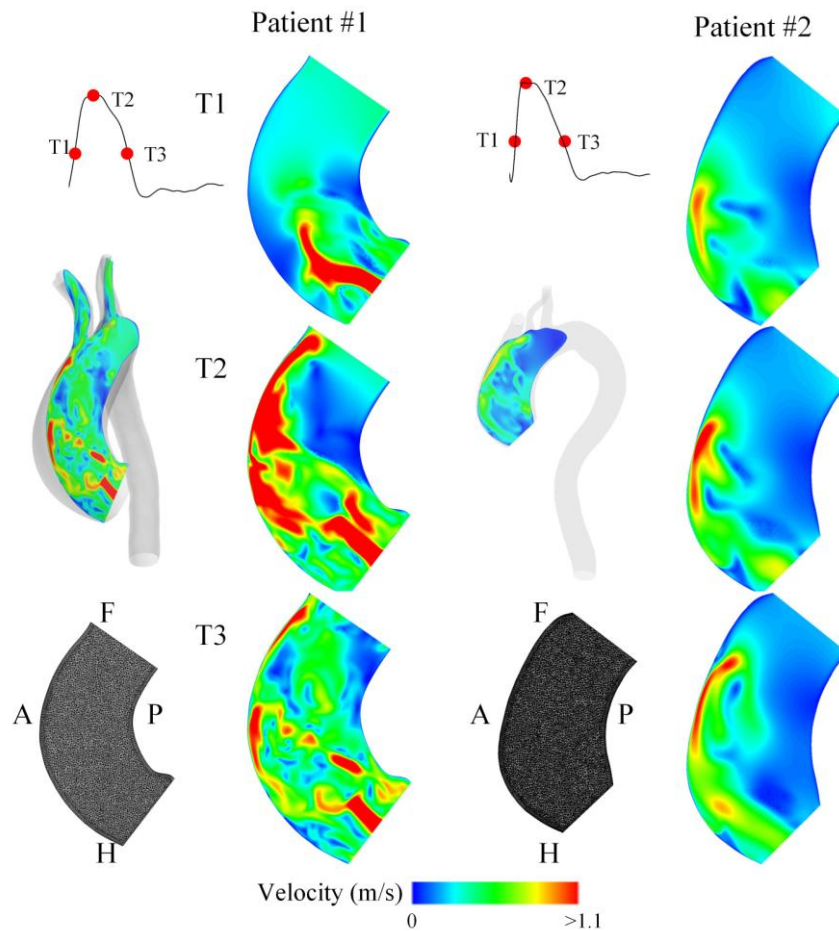


Figure 7. Simulated flow fields (illustrated in form of filled flow velocity contours in a longitudinal cutting plane at three time moments (i.e., T1, T2 and T3)) in the aortas of patient #1 (left panel) and patient #2 (right panel).

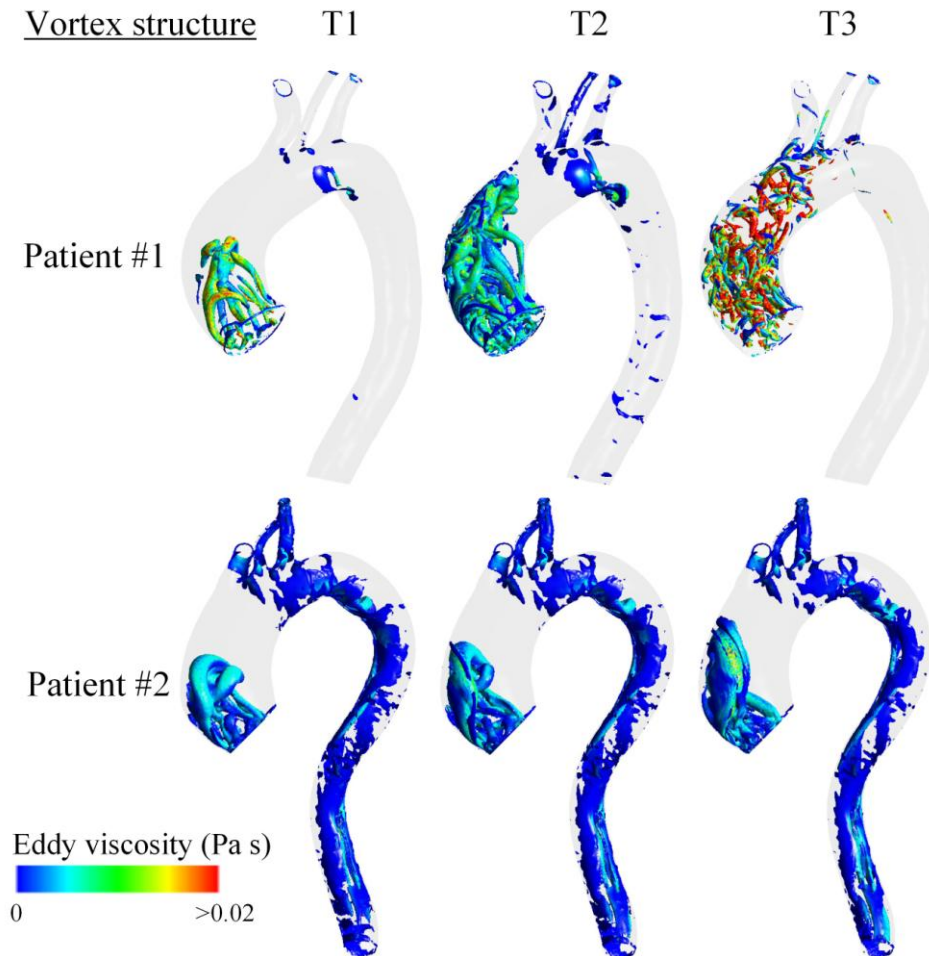


Figure 8. Vortex structures represented by iso-surfaces of Λ_2 at a level value of 0.05 colored by the turbulent eddy viscosity at three time moments (i.e., T1, T2 and T3) in the aortas of patient #1 (upper panel) and patient #2 (lower panel).

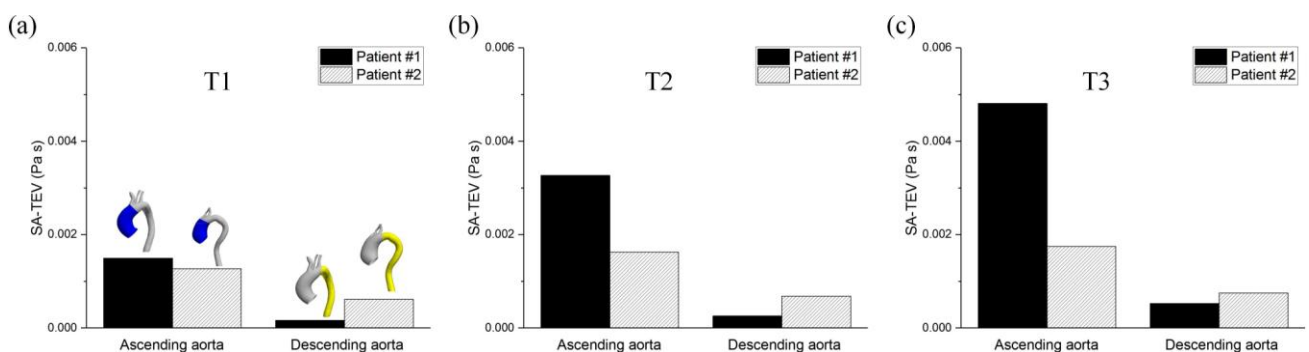


Figure 9. Comparisons of the simulated SA-TEV in the ascending and descending aortic segments (denoted by blue and yellow in the geometrical models) at three time moments (i.e., T1, T2 and T3) between patient #1 and patient #2.

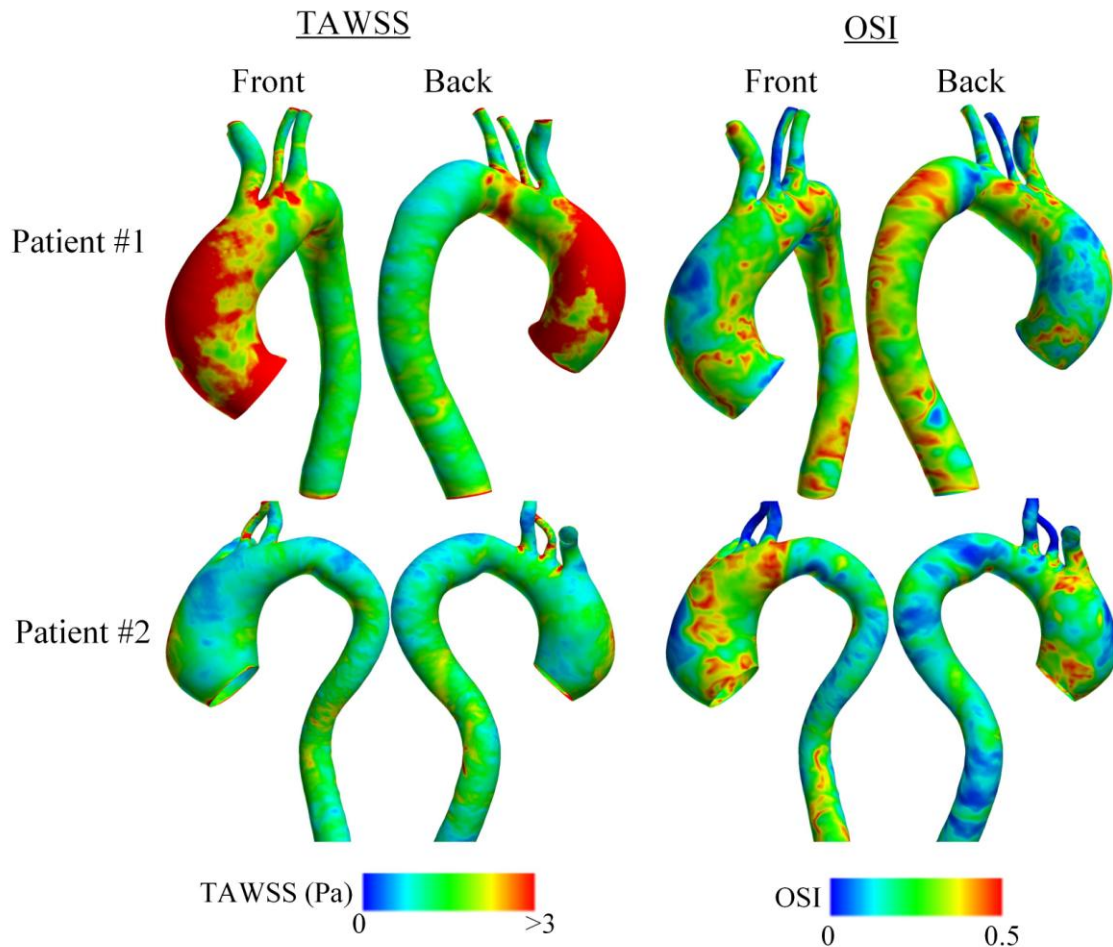


Figure 10. Simulated distributions of TAWSS and OSI in the aortas of patient #1(left panel) and patient #2 (right panel).

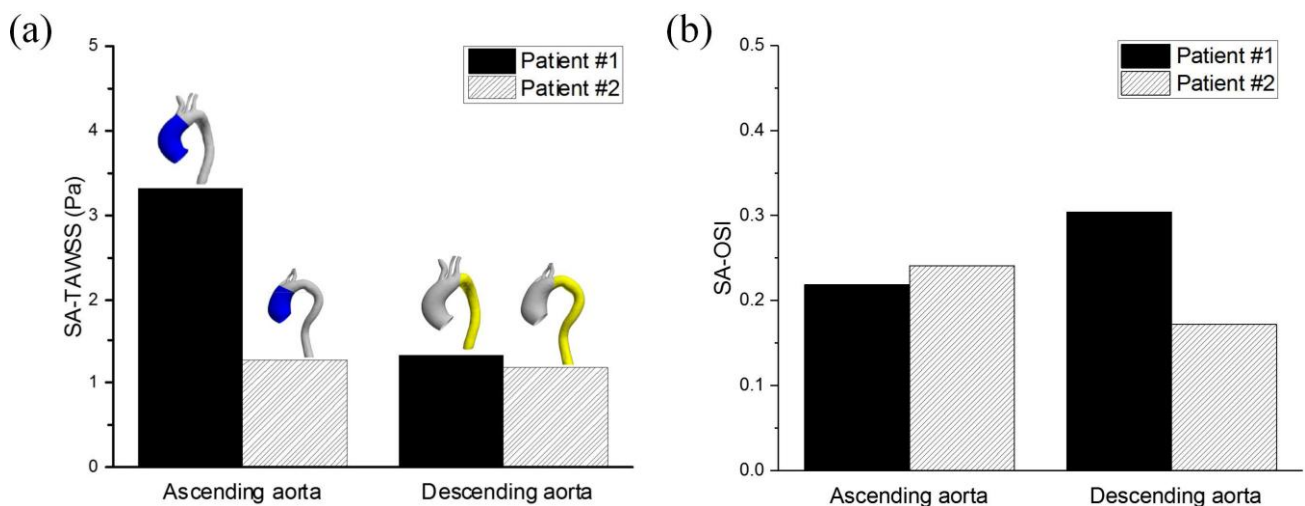


Figure 11. Comparisons of the simulated SA-TAWSS (a) and SA-OSI (b) in the ascending and descending aortic segments (denoted by blue and yellow respectively in the geometrical models) between patient #1 and patient #2.

4. Discussion

In the present study, blood flows in two aortas with pathological dilation of the ascending segment while differential aortic valve conditions were numerically simulated and compared. The presence of high-speed eccentric jet flows and regional high WSS was predicted in the ascending aortic segment of both aortas. In comparison with the aorta with quasi-normal TAV, the aorta with RL-BAV had stronger and more widely distributed jet flows in the ascending aortic segment that caused a marked elevation of WSS at both the anterior and right walls. While most of these model-predicted hemodynamic features and their differences between the two aortas have been reported in previous studies on similar subtypes of aortic dilation and aortic valve disease [9–11], the adoption of the LES method for flow modeling in the study allowed us to further explore the intensity and spatial distribution of flow turbulence and their association with the morphotype and functional state of aortic valve.

Theoretically, the proximal portion (i.e., the ascending aortic segment) of aorta not only has complex inflow conditions due to the anatomical connection to the left ventricle via the aortic valve, but also has larger diameter and higher curvature/tortuosity in comparison with the distal portion [38], which together would render blood flow in the ascending aorta more complex and unstable than in the descending aorta, and especially more vulnerable to the influence of aortic valve function. It has been extensively demonstrated that the morphotype and functional state of aortic valve significantly affect flow patterns in the ascending aorta [9–14], and that dilation of the ascending aorta per se augments local flow disturbance by inducing larger flow helices and long-lasting retrograde flow [7]. With regard to the two aortas investigated in the present study, in comparison with the aorta (of patient #2) with quasi-normal TAV, the aorta (of patient #1) with RL-BAV had remarkably higher intensity and wider distribution of flow turbulence, stronger flow disturbance, and larger area of wall subject to elevated WSS in the ascending aortic segment. Given the fact that the mean Reynolds number at the aortic inlet (521 vs. 922) and the severity of aortic dilation (maximum-to-aortic-inlet diameter ratio: 1.18 vs. 1.37) were both lower in patient #1 than in patient #2 (see Table 1), the different aortic valve conditions may be a main causative factor for the observed differential hemodynamic characteristics and flow turbulence in the ascending aortas of the two patients. The presence of a severely stenotic and moderately regurgitant RL-BAV in patient #1 caused the distribution of high-speed flows at the aortic inlet to be more concentrated and asymmetric (see Figure 3(d)), which not only resulted in the enlargement of wall regions subject to high WSS, but also promoted the formation/breakdown of unstable vortices to induce laminar-turbulent transition and associated increase in turbulent eddy viscosity (TEV) in the ascending aorta. Relatively, hemodynamic characteristics in the descending aortic segment were overall less influenced by aortic valve conditions, as demonstrated by the low turbulent eddy viscosity (see Figure 9) and comparable space-averaged wall shear stress between the two aortas (see Figure 11), although OSI in patient #1 was considerably higher than in patient #2 due primarily to the increased diastolic retrograde flow (see Figure 3(a)) caused by aortic valve regurgitation in patient #1.

Both abnormally high WSS and flow disturbance have been suggested to exert negative influence on endothelial function and wall remodeling [39,40], therefore one may speculate that regionally elevated WSS and increased flow disturbance/turbulence resulting from aortic valve anomaly or disease may be involved in the initiation and progression of aortopathy. For instance, adverse alterations in extracellular matrix protein expression in the aortic wall exposed to elevated

WSS have been observed in patients with BAV [41,42]. Exposure of normal aortic tissue to BAV-induced abnormal aortic WSS was found to result in increased MMP-2 and MMP-9 expressions and MMP-2 activity, indicating the potential role of BAV hemodynamic stresses in mediating aortic medial degradation [43]. On the other hand, a recent longitudinal study showed that no clinically relevant anatomical remodeling of the ascending aorta was observed during 3-year follow-up in BAV patients compared against healthy volunteers in spite of the regionally elevated aortic WSS associated with BAV, which suggests that WSS alterations may contribute to the onset of aortopathy, but WSS-driven anatomical remodeling may be a very slow process [44]. In addition, the congenital nature of BAV and aortic dilation implies that the roles of genetics are indisputable [10]. In a sense, the cause-and-effect relationship between hemodynamic factors and aortic dilation seems to be highly complicated and remains inconclusive given the limited evidence available in current literature. To better understand the relationship, large-scale long-term longitudinal studies would be necessary.

The present study is subject to certain limitations. Firstly, only two aortas with dilation of the ascending segment and specific aortic valve conditions were investigated in the study. Given the extensively demonstrated high sensitivities of aortic hemodynamics to aortic morphology and BAV morphotype [9–14], the presented findings might not be fully applicable to other aortas with different anatomical features and/or aortic valve abnormalities, although the general finding regarding the increased ascending aortic flow complexity and flow turbulence associated with aortic valve disease should hold. Secondly, while the LES modeling method has been widely proved as a practical approach to compensating for the inherent limitation of laminar flow assumption-based method in accounting for flow turbulence [29,30], the assumptions introduced in the modeling of sub-grid turbulent eddies and the limited spatio-temporal resolution of computational model render the LES-based numerical results unable to fully represent all scales of turbulent eddies. To overcome the limitation, DNS may be an alternative [24,25], but would incur extremely high computational cost. Thirdly, aortic walls were assumed to be rigid in the study, which is physiologically non-rigorous. Previous studies have demonstrated that ignoring wall deformation in the simulation of aortic hemodynamics leads to considerable overestimate of WSS [45,46]. In addition, the adoption of rigid-wall assumption makes computer models inherently lack the ability to account for physiological variations in phase angle and shape of flow waveform along the aorta resulting from pulse wave propagation, reflection and superimposition in the aorta [47], which may considerably compromise the fidelity of hemodynamic simulation in the distal portion (e.g., descending aortic segment) of aorta when measured flow waveforms are imposed to upstream aortic inlet and branch arteries. Our study did show that the model-predicted and measured flow waveforms at the outlet of the descending aorta differed significantly, and accordingly the discrepancies between the model-predicted and 4D-MRI-measured flow streamlines seemed to be larger in the descending aortic segment than in the ascending segment. Although how wall deformation would affect the occurrence and intensity of flow turbulence in the aorta remains incompletely understood, modeling methods capable of accounting for wall deformation and its interaction with blood flow are no doubt necessary to further improve the fidelity of hemodynamic simulation, especially when a large portion of aorta is involved.

5. Conclusion

Blood flows in two patient-specific aortas with dilation of the ascending segment have been numerically simulated with the LES method to address how the morphotype and functional state of aortic valve would influence the characteristics of aortic hemodynamics. It was found that the presence of a severely stenotic and moderately regurgitant BAV resulted in marked enlargement of wall regions exposed to elevated WSS and enhancement of flow turbulence in the ascending aortic segment. Relatively, the aortic valve disease had much smaller influence on flow patterns in the descending aortic segment, although OSI was considerably elevated due to the increased diastolic retrograde flow caused by valve regurgitation. These findings suggest that aortic valve disease has profound influence on flow patterns in the ascending aorta and further studies would be required to address how hemodynamic alterations associated with aortic valve disease would affect the progression of aortopathy.

Acknowledgments

The study was supported by the National Natural Science Foundation of China (Grant no. 11972231, 11832003), the China Postdoctoral Science Foundation (Grant no. 2018M640385), and the SJTU Medical-Engineering Cross-cutting Research Project (Grant no. YG2015MS53, YG2017MS45).

Conflict of interest

The authors declare there is no conflict of interest.

References

1. J. B. Kim, M. Spotnitz, M. E. Lindsay, et al., Risk of aortic dissection in the moderately dilated ascending aorta, *J. Am. Coll. Cardiol.*, **68**(2016), 1209–1219.
2. S. Verma and S. C. Siu, Aortic dilatation in patients with bicuspid aortic valve, *N. Engl. J. Med.*, **370**(2014), 1920–1929.
3. E. M. Isselbacher, Thoracic and abdominal aortic aneurysms, *Circulation*, **111**(2005), 816–828.
4. P. W. Fedak, T. E. David, M. Borger, et al., Bicuspid aortic valve disease: recent insights in pathophysiology and treatment, *Expert Rev. Cardiovasc. Ther.*, **3**(2005), 295–308.
5. M. Ferencik and L. A. Pape, Changes in size of ascending aorta and aortic valve function with time in patients with congenitally bicuspid aortic valves, *Am. J. Cardiol.*, **92**(2003), 43–46.
6. R. S. Beroukhi, T. L. Kruzick, A. L. Taylor, et al., Progression of aortic dilation in children with a functionally normal bicuspid aortic valve, *Am. J. Cardiol.*, **98**(2006), 828–830.
7. T. A. Hope, M. Markl, L. Wigström, et al., Comparison of flow patterns in ascending aortic aneurysms and volunteers using four-dimensional magnetic resonance velocity mapping, *J. Magn. Reson. Imag.*, **26**(2007), 1471–1479.
8. A. J. Barker, P. Ooij, K. Bandi, et al., Viscous energy loss in the presence of abnormal aortic flow, *Magn. Reson. Med.*, **72**(2014), 620–628.
9. R. Mahadevia, A. J. Barker, S. Schnell, et al., Bicuspid aortic cusp fusion morphology alters

- aortic three-dimensional outflow patterns, wall shear stress, and expression of aortopathy, *Circulation.*, **129**(2014), 673–682.
10. N. Saikrishnan, L. Mirabella and A. P. Yoganathan, Bicuspid aortic valves are associated with increased wall and turbulence shear stress levels compared to trileaflet aortic valves, *Biomech. Model. Mechanobiol.*, **14**(2015), 577–588.
 11. N. Saikrishnan, C. H. Yap, N. C. Milligan, et al., In vitro characterization of bicuspid aortic valve hemodynamics using particle image velocimetry, *Ann. Biomed. Eng.*, **40**(2012), 1760–1775.
 12. A. McNally, A. Madan and P. Sucaskey, Morphotype-dependent flow characteristics in bicuspid aortic valve ascending aortas: a benchtop particle image velocimetry study, *Front Physiol.*, **8**(2017), 1–11.
 13. K. Cao, S. K. Atkins, A. McNally, et al., Simulations of morphotype-dependent hemodynamics in non-dilated bicuspid aortic valve aortas, *J. Biomech.*, **50**(2017), 63–70.
 14. K. Cao and P. Sucaskey, Effect of Bicuspid aortic valve cusp fusion on aorta wall shear stress: Preliminary computational assessment and implication for aortic dilation, *World J. Cardiovasc. Dis.*, **5**(2015), 129–140.
 15. P. Youssefi, A. Gomez, T. He, et al., Patient-specific computational fluid dynamics—assessment of aortic hemodynamics in a spectrum of aortic valve pathologies, *J. Thorac. Cardiovasc. Surg.*, **153**(2017), 8–20.
 16. F. Condemi, S. Campisi, M. Viallon, et al., Fluid- and biomechanical analysis of ascending thoracic aorta aneurysm with concomitant aortic insufficiency, *Ann. Biomed. Eng.*, **45**(2017), 1–12.
 17. L. Goubergrits, R. Mevert, P. Yevtushenko, et al., The impact of mri-based inflow for the hemodynamic evaluation of aortic coarctation, *Ann. Biomed. Eng.*, **41**(2013), 2575–2587.
 18. D. Gallo, F. Negri, D. Tresoldi, et al., On the use of in vivo measured flow rates as boundary conditions for image-based hemodynamic models of the human aorta: Implications for indicators of abnormal flow, *Ann. Biomed. Eng.*, **40**(2012), 729–741.
 19. U. Morbiducci, R. Ponzini, D. Gallo, et al., Inflow boundary conditions for image-based computational hemodynamics: impact of idealized versus measured velocity profiles in the human aorta, *J. Biomech.*, **46**(2013), 102–109.
 20. S. Pirola, B. Guo, C. Menichini, et al., 4D flow MRI-based computational analysis of blood flow in patient-specific aortic dissection, *IEEE Trans. Biomed. Eng.*, (2019), in press.
 21. S. Pirola, Z. Cheng, O. A. Jarral, et al., On the choice of outlet boundary conditions for patient-specific analysis of aortic flow using computational fluid dynamics, *J. Biomech.*, **60**(2017), 15–21.
 22. P. D. Stein and H. N. Sabbah, Turbulent blood flow in the ascending aorta of humans with normal and diseased aortic valves, *Circ. Res.*, **39**(1976), 58–65.
 23. A. F. Stalder, A. Frydrychowicz, M. F. Russe, et al., Assessment of flow instabilities in the healthy aorta using flow-sensitive MRI, *J. Magn. Reson. Imag.*, **33**(2011), 839–846.
 24. R. Mittal, S. P. Simmons and F. Najjar, Numerical study of pulsatile flow in a constricted channel, *J. Fluid Mech.*, **485**(2003), 337–378.
 25. C. Zhu, J. H. Seo and R. Mittal, Computational modelling and analysis of haemodynamics in a simple model of aortic stenosis, *J. Fluid Mech.*, **851**(2018), 23–49.
 26. N. H. Johari, N. B. Wood, Z. Cheng, et al., Disturbed flow in a stenosed carotid artery

- bifurcation: Comparison of RANS-based transitional model and LES with experimental measurements, *Int. J. Appl. Mech.*, **11**(2019), 4.
27. R. Agujetas, C. Ferrera, A. C. Marcos, et al., Numerical and experimental analysis of the transitional flow across a real stenosis, *Biomech. Model. Mechanobiol.*, **16**(2017), 1447–1458.
 28. F. P. P. Tan, N. B. Wood, G. Tabor, et al., Comparison of LES of steady transitional flow in an idealized stenosed axisymmetric artery model with a RANS transitional model, *ASME. J. Biomech. Eng.*, **133**(2011), 051001.
 29. M. Andersson, T. Ebbers and M. Karlsson, Characterization and estimation of turbulence-related wall shear stress in patient-specific pulsatile blood flow, *J. Biomech.*, **85**(2019), 108–117.
 30. J. Lantz, T. Ebbers, J. Engvall, et al., Numerical and experimental assessment of turbulent kinetic energy in an aortic coarctation. *J. Biomech.*, **46**(2013), 1851–1858.
 31. S. Karimi, M. Dabagh, P. Vasava, et al., Effect of rheological models on the hemodynamics within human aorta: CFD study on CT image-based geometry, *J. Non-Newton. Fluid Mech.*, **207**(2014), 42–52.
 32. R. E. Collins, *Flow of fluids through porous materials*, (1976).
 33. J. O. Hinze, *Turbulence. McGraw-Hill Publishing Co*, (1975).
 34. F. Nicoud and F. Ducros, Subgrid-scale stress modelling based on the square of the velocity gradient tensor, *Flow, Flow Turbul. Combust.*, **62**(1999), 183–200.
 35. P. Youssefi, A. Gomez, C. Arthurs, et al., Impact of patient-specific inflow velocity profile on hemodynamics of the thoracic aorta, *J. Biomech. Eng. Trans. ASME*, **140**(2018), 011002.
 36. L. Xu, F. Liang, L. Gu, et al., Flow instability detected in ruptured versus unruptured cerebral aneurysms at the internal carotid artery, *J. Biomech.*, **72**(2018), 187–199.
 37. Z. Zhang, L. Xu, R. Liu, et al., Importance of incorporating systemic cerebroarterial hemodynamics into computational modeling of blood flow in intracranial aneurysm, *J. Hydrodyn.*, (2019), 1–14.
 38. J. Alastruey, J. H. Siggers, V. Peiffer, et al., Reducing the data: Analysis of the role of vascular geometry on blood flow patterns in curved vessels, *Phys. Fluids*, **24**(2012), 031902.
 39. J. M. Dolan, J. Kolega and H. Meng, High wall shear stress and spatial gradients in vascular pathology: a review, *Ann. Biomed. Eng.*, **41**(2013), 1411–1427.
 40. D. Y. Lee, C. I. Lee, T. E. Lin, et al., Role of histone deacetylases in transcription factor regulation and cell cycle modulation in endothelial cells in response to disturbed flow, *Proc. Natl. Acad. Sci. USA*, **109**(2012), 1967–1972.
 41. M. Cotrufo, A. Della Corte, L. S. De Santo, et al., Different patterns of extracellular matrix protein expression in the convexity and the concavity of the dilated aorta with bicuspid aortic valve: preliminary results, *J. Thorac. Cardiovasc. Surg.*, **130**(2005), 504-e1.
 42. M. Bauer, V. Glicch, H. Siniawski, et al., Configuration of the ascending aorta in patients with bicuspid and tricuspid aortic valve disease undergoing aortic valve replacement with or without reduction aortoplasty, *J. Heart Valve Dis.*, **15**(2006), 594–600.
 43. S. K. Atkins, K. Cao, N. M. Rajamannan, et al., Bicuspid aortic valve hemodynamics induces abnormal medial remodeling in the convexity of porcine ascending aortas, *Biomech. Model. Mechanobiol.*, **13**(2014), 1209–1225.
 44. F. Piatti, F. Sturla, M. M. Bissell, et al., 4D flow analysis of BAV-related fluid-dynamic alterations: Evidences of wall shear stress alterations in absence of clinically-relevant aortic anatomical remodeling, *Front. Physiol.*, **8**(2017), 441.

45. M. Bonfanti, S. Balabani, M. Alimohammadi, et al., A simplified method to account for wall motion in patient-specific blood flow simulations of aortic dissection: Comparison with fluid-structure interaction, *Med. Eng. Phys.*, **58**(2018), 72–79.
46. M. Alimohammadi, J. M. Sherwood, M. Karimpour, et al., Aortic dissection simulation models for clinical support: fluid-structure interaction vs. rigid wall models, *Biomed. Eng. Online*, **14**(2015), 34.
47. F. Y. Liang, S. Takagi, R. Himeno, et al., Biomechanical characterization of ventricular–arterial coupling during aging: a multi-scale model study, *J. Biomech.*, **42**(2009), 692–704.



AIMS Press

©2020 the author(s), licensee AIMS Press. This is an open access article distributed under the terms of the Creative Commons Attribution License (<http://creativecommons.org/licenses/by/4.0>).